Defect-rich ruthenium dioxide electrocatalyst enabled by electronic reservoir effect of carbonized polymer dot for remarkable pH-universal oxygen evolution

Tanglue Feng [a,1], Jingkun Yu [b,1], Da Yue [a,1], Haoqiang Song [b], Songyuan Tao [a], Geoffrey I.N. Waterhouse [c], Siyu Lu [b,*], Bai Yang [a,*]

[a] State Key Laboratory of Supramolecular Structure and Materials, College of Chemistry, Jilin University, Changchun 130012, P.R. China
[b] Green Catalysis Center, and College of Chemistry, Zhengzhou University, Zhengzhou 450001, P.R. China
[c] School of Chemical Sciences, The University of Auckland, Auckland 1142, New Zealand

A B S T R A C T

Designing highly active and durable electrocatalysts for oxygen evolution reaction (OER) over a wide pH range is of great significance, but it remains challenging. Herein, a defect-rich RuO_2 electrocatalyst with pH-universal OER activity is developed by rationally utilizing the electronic reservoir effect of Mn-coordinated carbonized polymer dots (Mn-CPDs). Mn-CPDs as distinct electron acceptor/donor endows Ru-O sites of RuO_2 with abundant defective structures (i.e., O-Ru-O-Ru-Ru sites and O-Ru-O-Mn units) via reduction-oxidation processes, with incorporated Mn atoms simultaneously feeding electron to Ru. The resultant Ru-O-Mn/CPD exhibits an ultralow OER potential of 196 mV, 194 mV and 251 mV at 10 mA·cm^{-2} under 0.5 M H_2SO_4, 1.0 M KOH, and 1.0 M PBS media, respectively, and long-term catalytic stability, which are among the best OER electrocatalysts. Surprisingly, Ru-O-Mn/CPD also shows great Pt-like hydrogen evolution activity. The theoretical simulation indicates that defective Ru-O-Mn structures produce electron-rich Ru region and near-optimal Ru-4d/O-2p band center, thus optimizing the adsorption/desorption kinetics of key intermediates.

1. Introduction

The electrochemical oxygen evolution reduction (OER) plays important role in water splitting and many energy conversion technologies [1–3]. The four electron-four proton OER reaction is complicated and has sluggish kinetics, requiring highly efficient and durable electrocatalysts capable of operating in acid, neutral or alkaline conditions. In recent years, researchers have attempted to discover low-cost transition metal-based electrocatalysts for OER, especially in alkaline media [4–6]. Layered double hydroxides (LDHs) such as NiFe-LDH, bimetallic oxyhydroxides (e.g. Ni(Fe)OOH) and NiFe metal-organic frameworks (NiFe-MOF), which were grown on conductive substrates (such as nickel foam), can all achieve ultralow initial OER overpotentials and high current densities [7–11]. However, these materials offer poor activity/stability in acidic and neutral media. To date, the great OER electrocatalysts under various media are still Ir and Ru-based materials [12, 13]. RuO_2 shows greater activity than Ir/IrO_2 and far better durability

than Ru [14,15], but there is still a lot of room for improvement in terms of activity and stability. Some metal-doped RuO_2 catalysts [16–24] were reported to show excellent activity for acidic OER, but high-efficiency pH-universal OER activity for RuO_2 has still not been achieved.

To achieve efficient OER kinetics, regulating and optimizing the adsorption strength and desorption of key catalytic intermediates is essential. This requires precise manipulation on the electronic structure of metal sites in OER catalysts. Defect engineering is an effective strategy to modify the electronic structure of metal active sites for improved activity [2,25–27]. The OER activity of RuO_2 was also shown to greatly depend on the electronic/defective structure of Ru-O units [28]. In particular, oxygen vacancy defects were found to lower the energies of the O 2p band and Fermi level, enhancing the covalent nature of metal-oxygen bonding [29]. RuO_2-based electrocatalysts were typically fabricated through either direct high-temperature oxidation of Ru^{3+} precursor/carrier composites (such as metal-organic framework materials [17,18,30], polymer/small molecules [31–33], metal/nonmetal

substrates [34,35]), or low-temperature oxidation of colloidally prepared Ru (or alloy) nanoparticles [36]. These RuO_2 catalysts tend to have vitally well-ordered crystalline structures and a full Ru-O coordination shell (i.e., contain few defects) [28,37]. Engineering the electronic/defective structure of Ru-O units in RuO_2 thus requires alternative strategies. Researchers found that the construction of Ru-O-M-O units (M = Mn, Fe, Co, Ni, Cu, etc.) and the introduction of oxygen defects in RuO_2 could greatly enhance acidic OER activity by suppressing lattice oxygen participation [17–22,34,38]. However, the improved OER activity in these systems u for in-situ generated oxygen defects created by the etching effect of the acidic electrolyte [28]. Accordingly, this approach is not practical for OER in neutral/alkaline media or the hydrogen evolution reaction (HER). Therefore, it is highly desired to find a way to controllably engineer the electronic structure of Ru-O sites in RuO_2 electrocatalysts to achieve pH-universal OER activity, with HER activity being a further welcome bonus.

Carbonized polymer dots (CPDs) are an emerging class of carbon nanomaterial, possessing many desirable structural and electronic properties as building units of OER electrocatalysts, including large surface area, high conductivity, inherently abundant N, O-containing sites/functional groups (i.e., carbon defects), good electron donor/acceptor character, and excellent chemical stability [39–46]. The abundant functional/defective sites enable CPD to strongly coordinate metals [47,48], whilst the carbonized core allows controlled metal reduction/oxidation by serving as an electron reservoir. By this strategy, the coordination/defect structures of metal/metal-O sites can be exquisitely manipulated. The immobilization of metals such as Mn^{2+}, Co^{2+}, Cu^{2+}, Zn^{2+} on defective surface sites of CPDs creates metal-doped CPDs (M-CPDs), which often possess enhanced structural and electronic properties compared to pure CPDs and thus can be highly beneficial in electrocatalysis [49,50].

Herein, the rational designed Mn-CPDs with abundant functional sites and distinct electron reservoir character were employed to electrically couple Ru sites and to fabricate defect-rich RuO_2 electrocatalyst for pH-universal oxygen evolution via reduction-oxidation strategy. The as-fabricated Ru-O-Mn/CPD catalyst has abundant Ru-O defect structures in the RuO_2 lattice, including O-Ru-O-Ru-Ru sites and O-Ru-O-Mn units. X-ray absorption/photoelectron spectroscopy and theoretical simulations reveal that defective Ru-O sites caused significant Ru charge redistribution and optimized the Ru-4d/O-2p band center of the catalyst, thus improving the intermediate kinetics of HER/OER pathway. Consequently, Ru-O-Mn/CPD exhibits highly active and stable OER activity in 0.5 M H_2SO_4, 1.0 M KOH, and neutral 1.0 M PBS media with ultralow OER potentials at 10 mA·cm^{-2} of only 196 mV, 194 mV and 251 mV, respectively. Simultaneously, Ru-O-Mn/CPD shows great Pt/C-like hydrogen evolution activity. The proposed strategy paves a new pathway to designing an efficient pH-universal OER electrocatalyst.

2. Experimental sections

2.1. Chemicals

Cobalt gluconate ($C_{12}H_{22}CoO_{14}$·xH_2O) was purchased from Alfa Aesar. Zinc gluconate (98%), copper gluconate (98%), ferrous gluconate (98%), aqueous gluconate solution (49–53 wt%) and N,N-diethylaniline (DEA, 99%) were purchased from Macklin. Manganese gluconate (99%) was purchased from Changchun Sanbang Pharmaceutical Technology Co. Ltd. Tryptophan (AR, 99%), ruthenium trichloride hydrate ($RuCl_3$·xH_2O, 35.0–42.0 wt% Ru) and 2,4-dinitrotoluene (DNT, 99%) were purchased from Aladdin. The graphene oxide (GO) aqueous dispersion (1.02 wt%) and nitrogen-doped multi-walled carbon nanotubes (N-MWCNTs) were purchased from Changzhou Sixth Element Materials Co. Ltd and XFNANO, respectively.

2.2. Synthesis of materials

Metal ions-doped carbonized polymer dots (M-CPDs). In a typical synthesis of Mn-CPDs, 0.25 g of manganese gluconate and 0.3 g of tryptophan were dissolved in 10 mL deionized (DI) water, followed by ultrasonication for about 20 min. Next, the solution was transferred to an autoclave and hydrothermal treated at 200 °C for 6 h. After cooling naturally to room temperature, the product suspension was filtered through a 0.22 μm membrane to remove any large particles. The as-obtained yellow-brown aqueous dispersion contains the Mn-CPDs. The Mn-CPDs dispersion could be mixed directly with metal salts or dried at 60 °C to produce a yellow Mn-CPDs powder. The obtained Mn-CPDs powder could easily be redispersed in DI water for further characterization or other uses. The synthesis of CPDs doped with other metal ions (Cu-CPDs, Zn-CPDs, Co-CPDs, Fe-CPDs) was similar to the synthesis of Mn-CPDs, except that manganese gluconate was replaced with copper gluconate, zinc gluconate, cobalt gluconate, or ferrous gluconate, respectively.

The synthesis of Ru-O-M/CPD catalysts. In a typical synthesis of Ru-O-Mn/CPD catalyst, 100 mg $RuCl_3$·xH_2O was dissolved in 10 mL of the Mn-CPDs dispersion, followed by ultrasonication for 30 min to achieve uniform dispersion. The Mn-CPD@Ru^{3+} composite dispersion was then dried at 60 °C for 24 h to obtain a powder. Subsequently, the powder was heated in a tube furnace to 900 °C at 5 °C min^{-1} under an argon atmosphere, then held at 900 °C for 4 h. After cooling to room temperature, a portion of the sample was calcined at 300 °C for 1 h in a static air atmosphere, using a heating rate of 5 °C min^{-1}. Next, 20 mg of the catalyst was dispersed in 45 mL of an aqueous 0.5 M H_2SO_4 solution and left to soak for 20 h. The dispersion was then centrifuged at 9500 rpm for 10 min, washed with DI water three times to thoroughly remove the sulfuric acid, then finally dried at 60 °C. The obtained black powder is denoted herein as the Ru-O-Mn/CPD catalyst. The syntheses of the Ru-O-M/CPD catalysts (M = Cu, Zn, Fe, Co) were similar to that of Ru-O-Mn/CPD, except that Mn-CPDs were replaced by Cu-CPDs Zn-CPDs, Fe-CPDs or Co-CPDs. For the synthesis of the Ru-O-Zn/CPD catalyst, the annealing temperature was lowered to 850 °C in order to avoid Zn metal evaporation.

The synthesis of other control catalysts. (i) For the synthesis of Ru-Mn/CPD catalyst (section 1.2.2), the black powder obtained after high-temperature annealing at 900 °C for 4 h was used as a control catalyst (denoted herein as the Ru-Mn/CPD catalyst). (ii) The synthesis of the Ru-O/CPD catalyst was similar to the preparation of Ru-O-Mn/CPD, except that the manganese gluconate (250 mg) precursor used in the synthesis of Mn-CPDs was replaced with 50 wt% gluconic acid (441 mg). (iii) For the synthesis of Mn/O-Ru-O/CPD catalyst, the Mn-CPD@Ru^{3+} composite powder obtained after drying in section 1.2.2 (i.e., the powder before the calcination step) was placed in tube furnace and heated to 300 °C at 5 °C min^{-1} in static air atmosphere. After heating at 300 °C for 4 h, the product was allowed to cool naturally to room temperature. The sample was then treated with H_2SO_4, washed with water, and dried using the same procedure described above for the Ru-O-M/CPD catalysts. (iv) The pure Ru-O-Mn catalyst was synthesized by $NaBH_4$ reduction, followed by pyrolysis in the air. Typically, $RuCl_3$ (0.94 mmol) and $MnCl_2$ (0.11 mmol) precursors were added into 25 mL DI water, and the reaction was heated to 80 °C. Then, 5 mL of 5 wt% aqueous $NaBH_4$ was slowly added to the solution, and the temperature was kept at 80 °C for 2 h. After the reaction was cooled down to room temperature, the reaction mixtures were washed with DI water for several times, and then dried, with the black powder obtained. Finally, the black powder was pyrolyzed at 300 °C for 1 h in air atmosphere to obtain the pure Ru-O-Mn catalyst. (v) The pure Mn-doped RuO_2 catalyst was obtained by pyrolysis at 300 °C for 4 h in air atmosphere for the mixture of $RuCl_3$·xH_2O and $MnCl_2$ (with the molar ratio of 8.78: 1). (vi) Ru-O-Mn/N-CNTs and Ru-O-Mn/GO catalysts were synthesized in the same way as the Ru-O-Mn/CPD catalysts, except that Mn-CPDs were replaced by nitrogen-doped carbon nanotubes (N-CNTs) and graphene oxide (GO),

respectively, with the MnCl$_2$ added. The samples were then treated with H$_2$SO$_4$, washed with water, and dried using the same procedure described above for the Ru-O-M/CPD catalysts.

2.3. Characterization

TEM and HR-TEM images were obtained by transmission electron microscopy (JEM-2100 F) at 200 kV. High-angle annular dark-field scanning transmission electron microscopy (HAADF-STEM) images were collected on a spherical aberration-corrected transmission electron microscope (JEM-ARM300F) with a probe corrector at 300 kV. UV–vis absorption spectra were collected on a UV-3101PC spectrophotometer (Shimadzu). Photoluminescence spectra were obtained by using a 5301PC spectrophotometer (Shimadzu). The contents of carbon, nitrogen and hydrogen in samples were determined using an elemental analyzer (Elementar, Vario Micro Cube). The metal contents in samples were determined by inductively coupled plasma optical emission spectrometry (ELAN 9000/DRC). Infrared spectra were obtained on a Vertex 80 V Fourier transform infrared spectrometer (Brucker). X-ray photoelectron spectroscopy data were collected on an HP 5950 A ESCA system. XPS fitting of the high-resolution XPS spectra used XPS Peak software (Version 4.1). X-ray diffraction (XRD) patterns were obtained on an EMPYREAN powder X-ray diffractometer (Panalytical B.V.). Raman spectra were measured on a Labram HR Evolution Raman spectrometer (Horiba) equipped with a 633 nm excitation source. Nitrogen adsorption-desorption isotherms were obtained at 78 K using an adsorption analyzer (ASAP 2020, Micromeritics). Electron paramagnetic resonance (EPR) spectra were acquired on an EPR spectrometer. *In-situ* Raman spectroscopy under catalysis was measured by a modified electrochemical Raman cell that contain a three-electrode polyvinylidene fluoride cell with a sapphire window (0.5 mm thick) and a confocal Raman spectrometer (Renishaw inVia). The laser with an excitation wavelength of 532 nm and a power of 50 mW was used as the light source.

2.4. Electrochemical measurements

Preparation of working electrodes: 3.0 mg catalyst powder was dispersed in a mixed solution containing DI water (150 μL), ethanol (325 μL), and 25 μL of 5 wt% nafion solution, followed by ultrasonic treatment for 30–45 min in order to form a uniform catalyst ink. Subsequently, 6 μL of the catalyst ink was dripped onto the surface of a polished glassy carbon electrode (GCE) with a diameter of 3 mm.

All electrochemical tests were carried out on an electrochemical workstation (CHI660C) at room temperature, with the catalyst-modified GCE as the working electrode, a graphite rod as the counter electrode, and Hg/Hg$_2$Cl$_2$ or Hg/HgO as the reference electrode. The Hg/Hg$_2$Cl$_2$ reference electrode was used in quick tests conducted in 0.5 M H$_2$SO$_4$ or neutral 1.0 M PBS solution, whilst the Hg/HgO reference electrode was employed in 1.0 M KOH solutions. For long-term durability tests in acidic, neutral and alkaline electrolytes, the reference electrodes were Hg/Hg$_2$SO$_4$, Hg/Hg$_2$Cl$_2$ and Hg/HgO, respectively. Polarization curves were measured by linear sweep voltammetry (LSV) at the rate of 2 mV·s^{-1} without iR compensation. Electrochemical impedance spectroscopy data were collected in the frequency range from 100 mHz to 100 kHz at an AC amplitude of 5 mV. The Tafel slope was obtained by linear fitting according to the Tafel equation (η = A + B *log j). The electrochemical double layer capacitance (C$_{dl}$) and the corresponding electrochemical active surface area (ECSA) of the catalysts were determined by cyclic voltammetry (CV). Typically, a suitable voltage window was selected to measure the CV curves using different scanning rates (5–45 mV s^{-1}, with intervals of 5 mV s^{-1}). The sum of two absolute current density values at a potential in the middle of the voltage window was plotted versus the scanning rate. A linear fit was applied to the data, with the half of slope corresponding to the C$_{dl}$ value. All measured potentials were converted into the reversible hydrogen electrode (RHE) by

using the following equations: ERHE = EHg/Hg$_2$Cl$_2$ + 0.0591 *pH + 0.241 V, ERHE = EHg/Hg$_2$SO$_4$ + 0.0591 *pH + 0.616 V, ERHE = EHg/HgO + 0.0591 *pH + 0.098 V.

2.5. Density functional theory (DFT) simulation

A first-principles method was employed to calculate the geometry and electronic structure of the catalysts. All the calculations were performed using the projector augmented wave (PAW) formalism of density functional theory (DFT) as implemented in the Vienna Ab-initio Simulation Package (VASP) [1,2]. The exchange-correlation functional adopted the expression of Perdew-Burke-Ernzerhof (PBE) in the generalized gradient approximation (GGA) method [3]. Models were built based on the RuO$_2$ (101) surface, with the vacuum thickness at 15 Å in order to separate any two adjacent particles from lattice coupling. The energy cutoff for the plane-wave expansion was 400 eV for all the calculations. All structures were optimized with a convergence criterion of 1 × 10^{-5} eV for the energy and 0.02 eV Å^{-1} for the forces. A Monkhorst-Pack 3 × 3 × 1 k-point grid was used to sample the Brillouin zone for structure optimization. Based on a computational hydrogen electrode model introduced by Nørskov et al. [4], the Gibbs free energy was defined by the following equation:
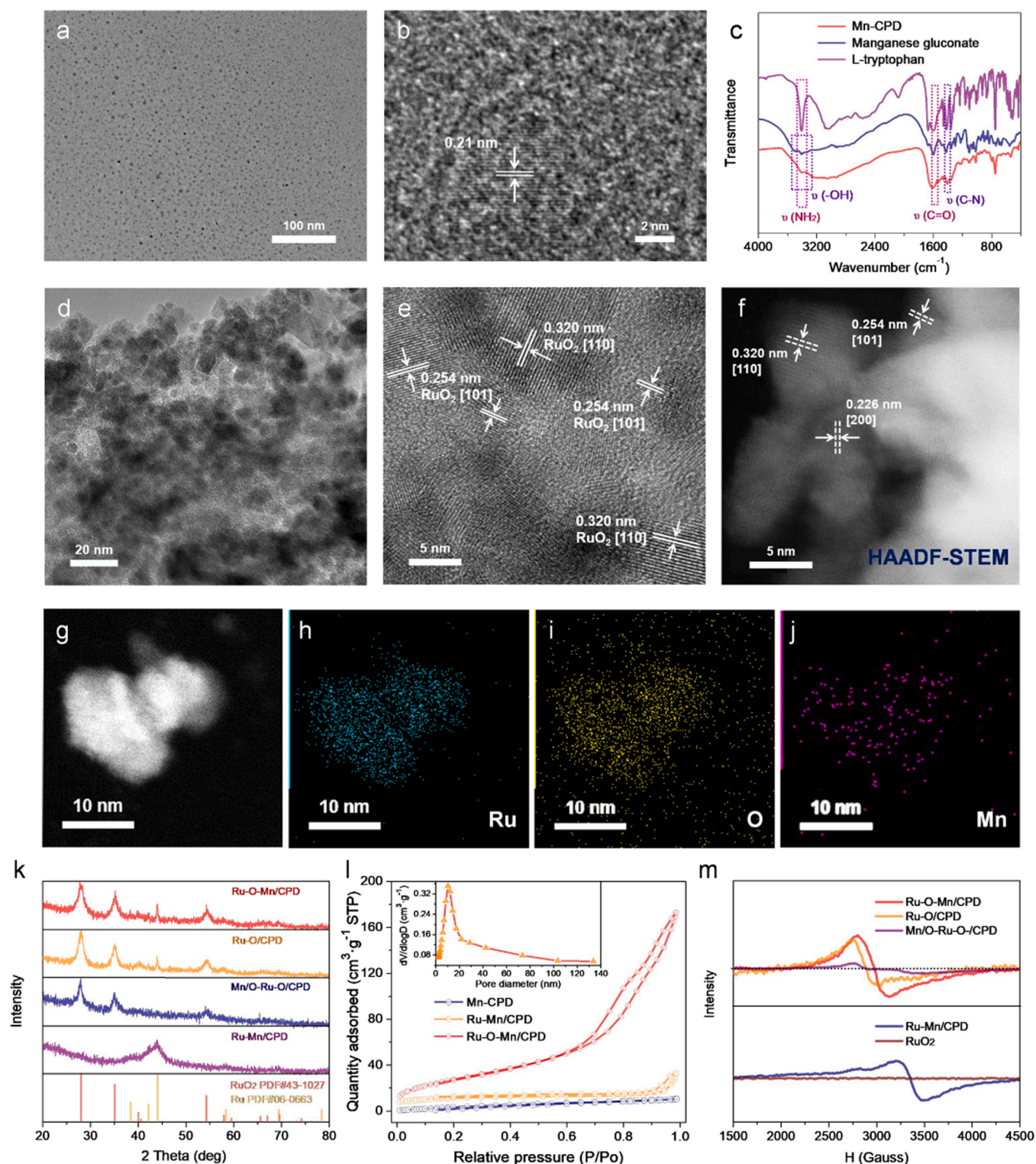
$$\Delta G = \Delta E + \Delta ZPE - T\Delta S$$

Where ΔE is the total energy difference between reactants and products of reactions, ΔZPE is the zero-point energy correction, ΔS is the vibrational entropy change at finite temperature T.

3. Results and discussion

3.1. Catalyst synthesis and structure characterization

The fabrication of ruthenium-oxygen-site (Ru-O-Mn/CPD) catalyst for pH-universal OER used metal-coordinated carbonized polymer dots (M-CPDs) the carrier and interfacial modifier of RuO$_2$. The Ru-O-Mn/CPD catalyst was obtained using a controlled reduction-oxidation pyrolysis approach as described in the experimental section. The M-CPD (M = Mn, Cu, Zn, Fe, Co) were ingeniously prepared from gluconate metal salt and tryptophan via hydrothermal process. The composition and electronic structure of representative Mn-CPDs were investigated in detail. Transmission electron microscopy (TEM) image (Fig. 1a) shows that the Mn-CPDs were spherical with an average particle size of about 5.0 nm. High-resolution TEM (HR-TEM) imaging of the Mn-CPDs (Fig. 1b) shows lattice fringes with a spacing of 0.21 nm corresponding to the interplanar spacing of graphene [100] facets. The UV–vis absorption and excitation-dependent photoluminescence spectra (Fig. S1) of Mn-CPDs confirm the successful formation of luminescence CPDs. Fourier transform infrared spectroscopy (FT-IR, Fig. 1c) reveals the Mn-CPDs to contain an abundance of -NH$_2$, -OH, C=O and C-N functional groups, thus inheriting much of the functionality of the precursors. High-resolution X-ray photoelectron spectroscopy (XPS) spectra validated the FT-IR results. The C 1s and O 1s regions (Fig. S2a,b) show various carbon and oxygen species, whilst the N 1s region (Fig. S2c) for Mn-CPDs is dominated by pyrrolic-N species from the tryptophan precursor. The Mn 2p XPS spectrum (Fig. S2d) shows that Mn in CPDs was in the form of coordinated ions (predominantly Mn^{2+} with corresponding Mn^{2+} shake-up satellites). These results suggest that as-prepared Mn-CPDs intrinsically contain plenty of N, O-containing functional group, which endow Mn-CPD with distinct electron-reservoir characters, i.e., electron donor/acceptor properties. From the fluorescence experiments (Fig. S3), the representative electron acceptor (DNT) and electron donor (DEA) both can effectively quench the fluorescence of Mn-CPD, which verifies the electron donor and electron acceptor characters of Mn-CPD, respectively. Electron paramagnetic resonance (EPR) spectrum of the Mn-CPDs displays a strong signal at g= 2.0015

Fig. 1. (a) TEM and (b) HR-TEM images of the as-prepared Mn-CPDs. (c) FT-IR spectra for Mn-CPDs and the two precursors. (d) TEM and (e) HR-TEM images, (f, g) HAADF-STEM image and (h-j) corresponding EDS mapping images of the Ru-O-Mn/CPD catalyst. (k) XRD patterns of Ru-O-Mn/CPD and other control catalysts. (l) Nitrogen adsorption/desorption isotherms for Mn-CPDs, Ru-Mn/CPD and Ru-O-Mn/CPD. Inset: corresponding pore size distribution of Ru-O-Mn/CPD catalyst. (m) EPR spectra of Ru-O-Mn/CPD catalysts and control samples.

(Fig. S4), further verifying the defective structures of Mn-CPDs. The high-density of metal binding sites, surface Mn-doping states and distinct electron donor/acceptor properties of the Mn-CPDs, were expected to offer a rich platform for the development of defective Ru-based OER catalysts.

Subsequently, the defective Mn-CPD was electrically coupled with Ru precursor to prepare RuO₂ catalyst (representatively denoted as Ru-O-Mn/CPD) by controllable reduction-oxidation pyrolysis procedures. Ru-Mn/CPD as the oxidative precursor for Ru-O-Mn/CPD fabrication was initially fabricated through the CPD-assisted reduction process.

During catalyst fabrication, Mn(II) atoms dopped in the original CPD are also firstly reduced and then oxidized into Mn(0) and oxidized Mn states, which were doped into the crystal lattices of Ru(0) and RuO$_2$, respectively. Other Ru-O-M/CPD catalysts (M = Cu, Zn, Fe, Co) were also synthesized using a similar reduction-oxidation process with Cu-CPDs, Zn-CPDs, Fe-CPDs and Co-CPDs, respectively, as building blocks (see methods section). The morphology and crystalline structure of the various catalysts were characterized by TEM, HR-TEM and spherical aberration correction TEM. The TEM and HR-TEM images of Ru-Mn/CPD in Fig. S5 show a uniform distribution of Ru metal nanoparticles (NPs) with an average size of 4.0 nm. The interplanar spacings corresponding to hexagonal closely packed (hcp) Ru and CPD can be observed. For the Ru-O-Mn/CPD catalyst, TEM image (Fig. 1d) reveals uniformly dispersed RuO$_2$ NPs with an average particle size of about 8.0 nm. An increase in particle size is found during the oxidation of metallic Ru nanoparticles into RuO$_2$. For the Ru-O-Mn/GO and Ru-O-Mn/N-CNTs control catalysts, nanoparticles were non-homogeneously distributed over the supports, with serious aggregation occurring (Fig. S6). This highlights the advantages of the Mn-CPDs-assisted reduction-oxidation strategy used here for inhibiting excessive growth and aggregation of RuO$_2$ NPs during catalyst fabrication. The HR-TEM image of the Ru-O-Mn/CPD catalyst (Fig. 1e) shows the lattice fringes with spacings of 0.320 nm and 0.254 nm, corresponding to the [110] and [101] interplanar spacings of RuO$_2$, respectively. No fringes due to hcp-Ru metal were found in the region imaged. High-angle annular dark field scanning TEM (HAADF-STEM) analysis of the Ru-O-Mn/CPD catalyst (Fig. 1f and Fig. S7a) further confirms the clear profile and uniform distribution of RuO$_2$ NPs. Energy dispersive X-ray spectroscopy (EDX, Fig. S7b) manifests that the contents of Ru, O and Mn atoms are 44.9, 31.9 and 2.12 wt%, respectively. The corresponding elemental mapping images (Fig. 1g-j, S8) reveal that Ru, O and Mn atoms were homogeneously distributed in the RuO$_2$ nanoparticles. TEM and HR-TEM images of Mn-free Ru-O/CPD in (Fig. S9) suggest that Mn-doping in Ru-O site has a negligible effect on the morphology and crystalline structure of the catalysts.
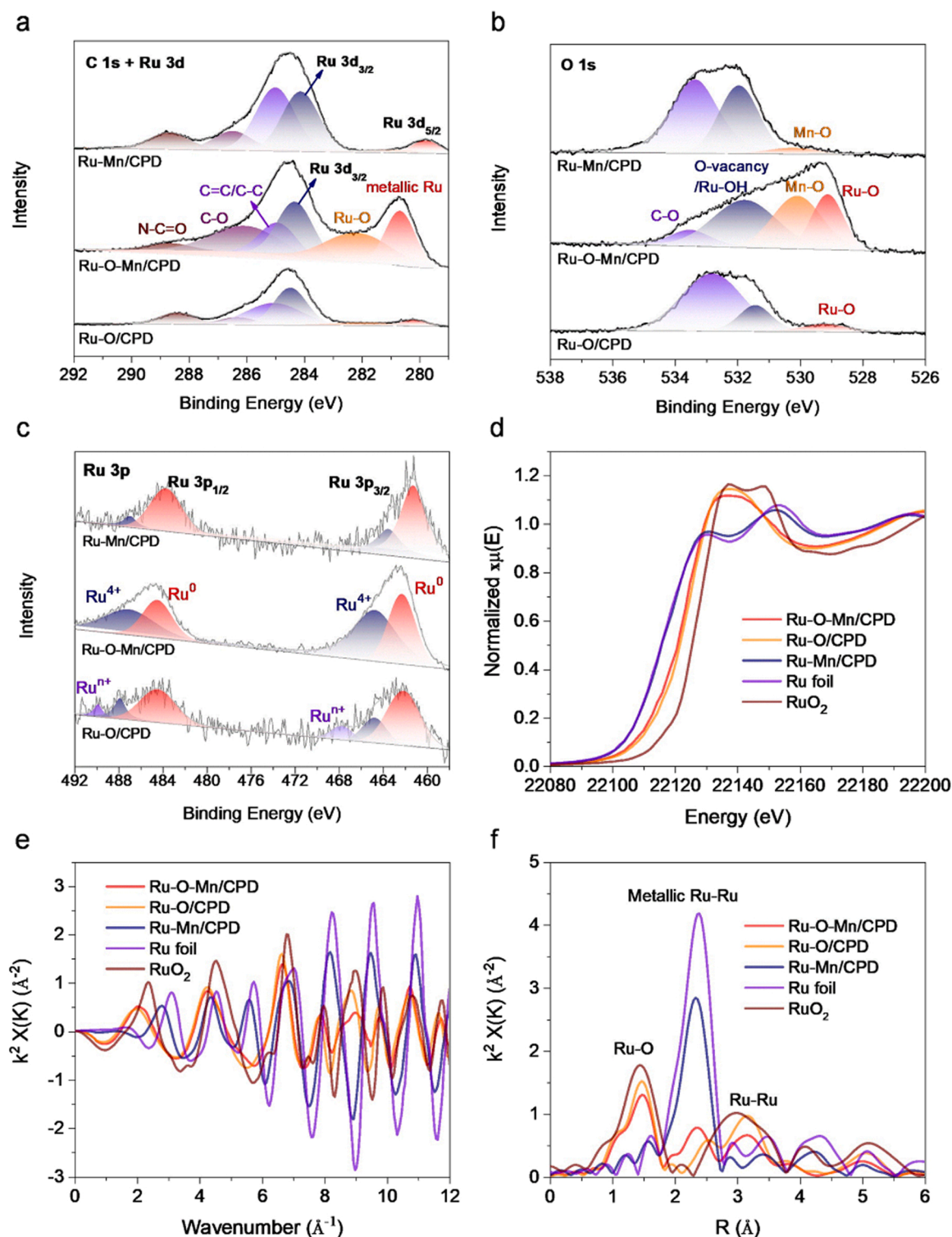
Furthermore, XRD (Fig. 1k) was used to explore the phase composition and crystalline structure of the catalysts. For Ru-Mn/CPD, broad peaks were observed due to reflections from small Ru NPs, and no evidence for alloying between Ru and Mn, or the presence of RuO$_2$, was found. The XRD pattern of Ru-O-Mn/CPD shows strong diffraction signals at 28.0, 35.1 and 54.3° corresponding to the (110), (101) and (211) planes of tetragonal RuO$_2$ (PDF# 43–1027), respectively, which is similar as commercial RuO$_2$ (Fig. S10). Compared to XRD pattern of Mn/O-Ru-O/CPD synthesized by direct oxidation from Ru^{3+}/Mn-CPD, Mn-CPD-assisted controllable reduction-oxidation strategy allowed Ru-O-Mn/CPD to retain a weak diffraction signal at 44.0° corresponding to [101] facet of hcp Ru. The Ru signal gradually decreased with CPD content increased as shown in Fig. S11, suggesting that CPDs can promote Ru metal oxidation to convert into Ru-O sites during reduction-oxidation process. The retentive small amounts of Ru-Ru sites in Ru-O sites could generate defective structures in Ru-O-Mn/CPD. Additionally, we hypothesize that the anchored Mn sites from CPDs create Ru-O-Mn-O units in the catalyst, thereby introducing a specific type of oxygen defect in the Ru-O sites. Interestingly for the Ru-O-Mn/GO and Ru-O-Mn/N-CNTs, there were almost no diffraction signals of RuO$_2$ in XRD (Fig. S12), even at a high oxidation temperature (500 °C). However, highly crystalline RuO$_2$ could be obtained at calcination temperatures ranging from 250 °C to 500 °C (Fig. S13) for Ru-O-Mn/CPD, which were attributed to the electron acceptor character of O-containing defective sites in CPDs. Besides, increasing calcination temperature favors the formation and crystallization of RuO$_2$ for Ru-O-Mn/CPD. XPS results demonstrate that as the calcination temperature increased, Ru and Mn valency increased (Fig. S14) and the oxygen vacancy amount can be manipulated (Fig. S15).

The contents of Ru and Mn in the Ru-O-Mn/CPD catalyst were determined to be 41.4 wt% and 2.56 wt%, respectively by inductively coupled plasma optical emission spectroscopy (ICP-OES), in excellent accord with the EDX results. The C, N, and H contents in the samples decreased on going from Mn-CPDs to Ru-Mn/CPD and finally Ru-O-Mn/CPD (Table S1), with the latter only containing 5.20 wt% C and 0.1 wt% N. Correspondingly, nitrogen adsorption-desorption isotherms (Fig. 1l, Table S2) show the specific surface area is increased from 38.3 m$^2 \cdot$g^{-1} for Ru-Mn/CPD to 103.1 m$^2 \cdot$g^{-1} for Ru-O-Mn/CPD), thus offering abundant catalytic reaction sites and charge transfer channels for OER. The presence of RuO$_2$ in Ru-O-Mn/CPD was confirmed by Raman spectroscopy (Fig. S16). Electron paramagnetic resonance (EPR) spectra for Ru-O-Mn/CPD, Ru-O/CPD, and Mn/O-Ru-O-/CPD (Fig. 1m) show broad EPR signals attributable to Ru-O defects. Typically, Ru-O/CPD displays an obvious EPR signal, and the Mn incorporation can further enhance signal intensity, with the g factor decreased. The Ru-Mn/CPD sample shows an EPR signal at g= 2.0015 due to defect structures in the original CPDs, whilst pure commercial RuO$_2$ shows no EPR signal. These results indicate that there are two types of defects, which originate from the existence of Ru-Ru sites and oxidized Mn sites in RuO$_2$ lattice, respectively. Such defects were expected to alter the charge distribution and band center of Ru-O sites and affect the adsorption of OER intermediates.

The near-surface region electronic structures of the catalysts were probed by XPS. The high-resolution C 1 s and Ru 3d spectra (Fig. 2a) revealed abundant oxygen-associated species (defect sites) in Ru-Mn/CPD including N-C=O (288.67 eV) and C-O (286.47 eV), which were able to couple with Ru/Mn(0) sites and allow controlled oxidation into Ru-O-Mn sites during the synthesis of Ru-O-Mn/CPD. The strong Ru-O (282.18 eV) and metal Ru (280.66 eV) states can be both observed in Ru-O-Mn/CPD, indicating the formation of O-Ru-O-Ru-Ru structures. In addition, Ru-O signal of Ru-O-Mn/CPD catalyst moves towards a higher binding energy position compared to that of Ru-O/CPD due to the strong electronic coupling of Ru-O-Mn. The O 1 s spectrum (Fig. 2b) of Ru-O-Mn/CPD could be deconvoluted into lattice oxygen species (Ru-O, 529.1 eV; Mn-O, 530.1 eV), Ru-OH/O-vacancy (531.8 eV) and C-O species (533.5 eV). The oxygen defect signal in Ru-O-Mn/CPD was notably increased compared with Ru-O/CPD, meaning more unsaturated Ru sites formed owing to the Ru-O-Mn units. The Ru 3p spectrum (Fig. 2c) the Ru-O-Mn/CPD catalyst were deconvoluted into contributions from Ru^0 metal (462.27 eV and 484.47 eV) and Ru^{4+} species (464.72 eV and 487.04 eV). Ru-O-Mn/CPD contained significantly more Ru^{4+} than Ru-Mn/CPD, consistent with the oxidation or Ru metal to RuO$_2$. For the Mn-free catalyst, Ru-O/CPD, the Ru 3 p signals for oxides were observed at higher binding energies than that for Ru-O-Mn/CPD, suggesting that Ru-O-Mn units can restrict the formation of unstable high-valence (above +4) species and thus improve catalytic durability. The Mn 2p spectra (Fig. S17) show that the valence state of Mn atoms increased during the oxidation of Ru-Mn/CPD to Ru-O-Mn/CPD.

Furthermore, more accurate bulk information about valence states and coordination structures of catalyst in the different catalysts were obtained using Ru K-edge X-ray absorption spectroscopy (XAS). Fig. 2d displays Ru K-edge X-ray absorption near edge structure (XANES) of the catalysts. The spectra for Ru-O-Mn/CPD and Ru-O/CPD were similar to the RuO$_2$ reference with the transition from Ru 1 s to 5p orbitals at 22,130 eV observed, implying the presence of predominantly Ru-O species in these catalysts. The spectrum of the Ru-Mn/CPD catalyst resembles the Ru foil, indicating the predominance of Ru^0 in the catalyst. From the edge absorption energy (Fig. S18) of XANES spectra, the average Ru valence in Ru-Mn/CPD, Ru-O-Mn/CPD and Ru-O/CPD was fitted to be + 0.25, + 1.73, + 2.3, respectively. The slightly lower Ru oxidation state in Ru-O-Mn/CPD compared to Ru-O/CPD is attributed to an electron-donating effect of Mn atoms through Ru-O-Mn units. Ru K-edge extended X-ray absorption fine structure (EXAFS) was next used to explore the local coordination of Ru in the catalysts. Fig. 2e shows that the EXAFS spectra possessed a good noise-signal ratio. The Fourier-transformed (FT) EXAFS spectrum (Fig. 2f) of pure RuO$_2$ shows the peak at 1.44 Å due to a Ru-O first coordination shell. while the values for

Fig. 2. High-resolution XPS spectra for the Ru-O-Mn/CPD catalyst and control catalysts. (a) C 1 s and Ru 3d regions, (b) O 1 s region, and (c) Ru 3p region. (d) Ru K-edge XANES spectra, (e) EXAFS oscillations and (f) Ru K-edge Fourier transformed EXAFS spectra in R-space for Ru-O-Mn/CPD, Ru-O/CPD, Ru-Mn/CPD, Ru foil and pure RuO_2.

Ru-O/CPD and Ru-O-Mn/CPD are increased to 1.47 Å and 1.48 Å, respectively, which are consistent with the order of absorption energy in XANES. Ru-O-Mn/CPD and Ru-O/CPD also show a Ru-Ru signal similar to Ru foil, suggesting the presence of O-Ru-O-Ru-Ru structures. Fitting results for the EXAFS spectra, including coordination numbers and interatomic distances, are summarized in Fig. S19 and Table S3. The Ru-O, Ru-Ru and Ru-Mn b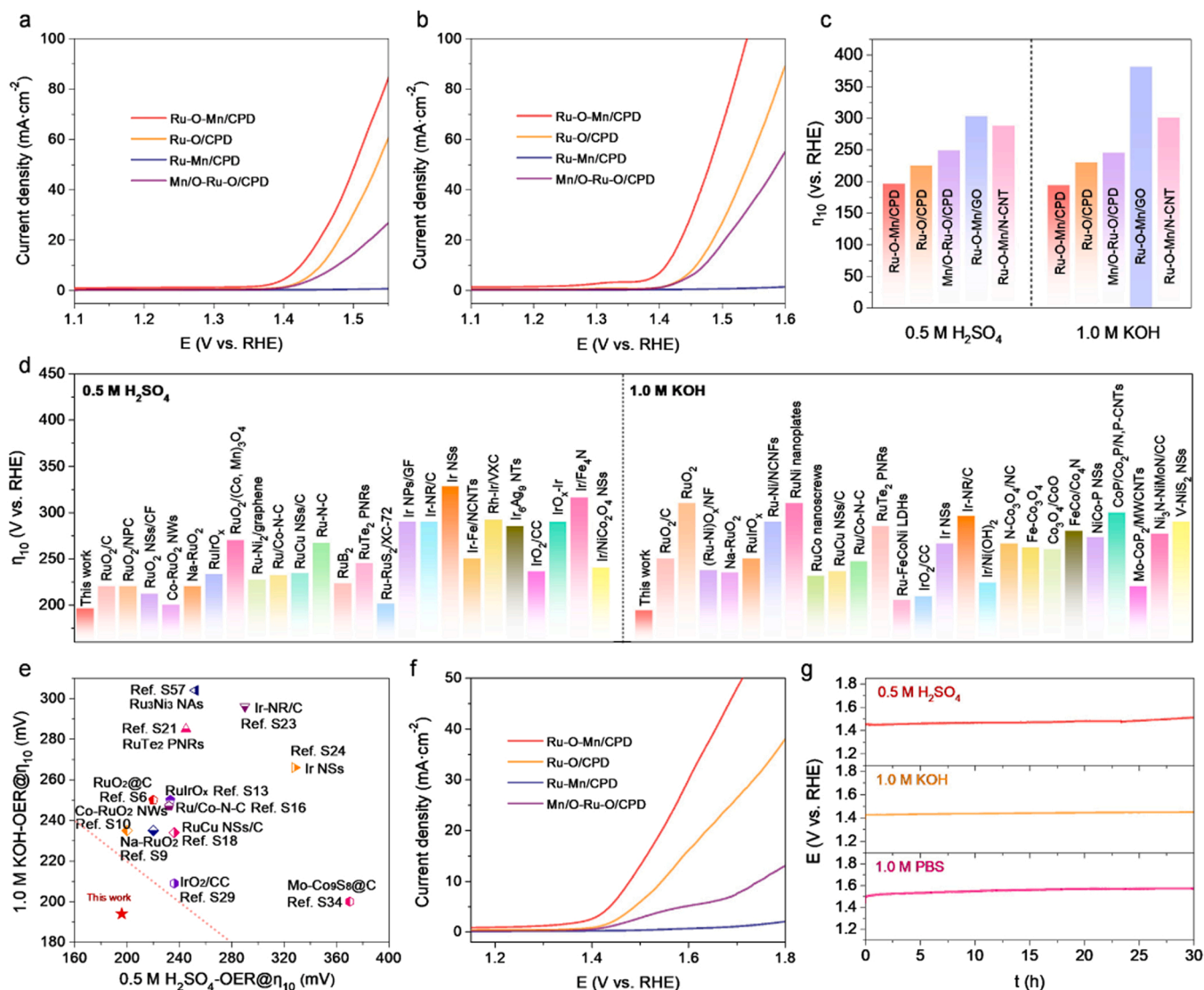onds were found in Ru-O-Mn/CPD. The Ru-O coordination numbers were fitted to be 5.12, 5.96 and 6 for Ru-O-Mn/CPD, Ru-O/CPD and RuO_2, respectively, confirming abundant defective Ru-O sites in Ru-O-Mn/CPD. Correspondingly, the x value of defective RuO_x lattice in Ru-O-Mn/CPD is calculated to be in a range from 1.5 to 1.9. The XAS supports two types of defective structures in Ru-O-Mn/CPD (i.e., O-Ru-O-Ru-Ru and Ru-O-Mn-O). Such defective Ru-O structures and Ru charge state were expected to give Ru-O-Mn/CPD

excellent OER performances.

3.2. Electrocatalytic activity of Ru-O-Mn/CPD

Subsequently, the electrochemical oxygen evolution (OER) performances of Ru-O-Mn/CPD and the other catalysts were evaluated using a standard three-electrode system. We first investigated the effect of oxidation temperature on OER performance of Ru-O-Mn/CPD catalyst, with Ru-O-Mn/CPD-300°C demonstrating the best OER activity (Fig. S20) due to the small grain size, strong crystallinity and the existence of many Ru-Ru sites and oxygen vacancies (Fig. S13-15). Moreover, polarization curves in Fig. 3a,b exhibit OER activities of Ru-O-Mn/CPD and control catalysts (Ru-O/CPD, Ru-Mn/CPD and Mn/O-Ru-O/CPD) in 0.5 M H_2SO_4 and 1.0 M KOH solution, with their overpotentials at 10 mA·cm^{-2} (η_{10}) shown in Fig. 3c. The Ru-O-Mn/CPD catalyst delivered the best OER activity, with ultralow overpotentials (η_{10}) of 196 mV and 194 mV in 0.5 M H_2SO_4 and 1.0 M KOH, respectively. Such OER activities in acidic and alkaline media are superior to all previously reported Ru-based, Ir-based and non-noble metal OER catalysts (Fig. 3d, Table S4,5). Catalysts with outstanding activity under both acidic and alkaline media are seldom reported in the literature (Fig. 3e), making the performance of Ru-O-Mn/CPD very exciting to the OER community. Interestingly, the Ru-O/CPD and Mn/O-Ru-O/CPD catalysts also show very good OER activity with a η_{10} of 225 mV and 249 mV in 0.5 M H_2SO_4, and 230 mV and 245 mV in 1.0 M KOH media, respectively. but such activities were inferior to Ru-O-Mn/CPD. This indicates that O-Ru-O-Ru-Ru and Ru-O-Mn units are both excellent OER sites, and act synergistically to enhance the catalytic activity of Ru-O-Mn/CPD. Other control catalysts (Ru-Mn/CPD, Ru-O-Mn/GO and Ru-O-Mn/N-CNTs) which contain plenty of metallic Ru-Ru sites (Fig. S12) show very poor OER activity (Fig. 3a,b, and Fig. S21). Therefore, Mn-CPDs-assisted reduction-oxidation (Ru^{3+} to Ru^0 to Ru-O) plays key roles in the electronic tuning at Ru-O sites of Ru-O-Mn/CPD for efficient OER activity. In addition, the Ru-O-Mn/CPD catalyst shows excellent OER activity in neutral 1.0 M PBS media (Fig. 3 f), with an ultralow overpotential (η_{10}) of 251 mV. The excellent OER performances of Ru-O-Mn/CPD over a wide pH range suggest great potential for application in efficient water splitting and fuel cells. Moreover, the OER durability of the Ru-O-Mn/CPD catalyst in acidic, alkaline and neutral media was next explored. Chronopotentiometry curve (Fig. 3g) shows that the OER
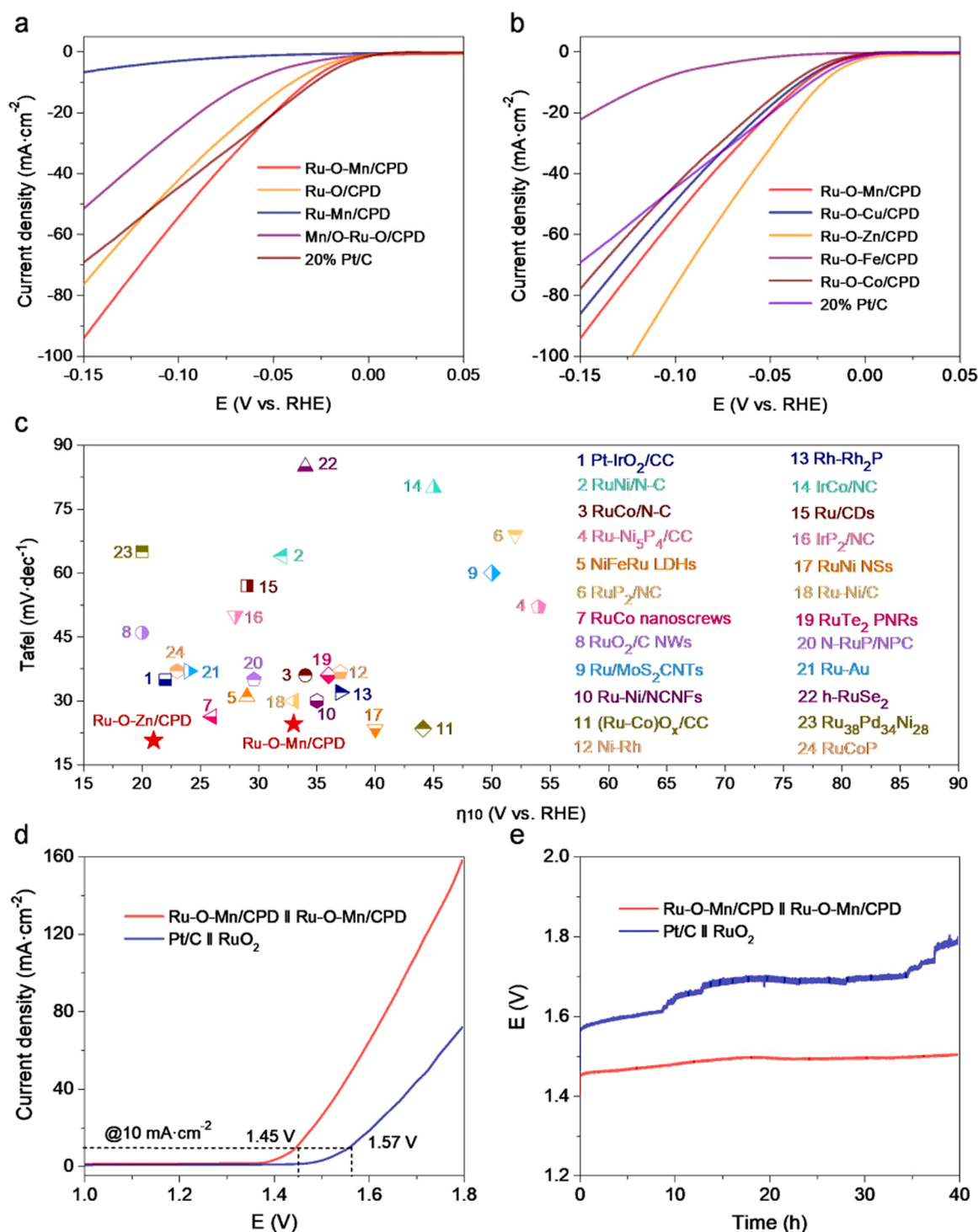

Fig. 3. Electrochemical OER performance of catalysts. (a, b) The polarization curves for Ru-O-Mn/CPD, Ru-O/CPD, Ru-Mn/CPD and Mn/O-Ru-O/CPD catalysts in 0.5 M H_2SO_4 and 1.0 M KOH, respectively. (c) OER activity comparison between Ru-O-Mn/CPD and control catalysts. (d, e) OER activity comparison between Ru-O-Mn/CPD and recently reported state-of-the-art OER catalysts in 0.5 M H_2SO_4 and 1.0 M KOH, respectively. (f) OER activity of the Ru-O-Mn/CPD and control catalysts in neutral 1.0 M PBS. (g) OER durability test for the Ru-O-Mn/CPD catalyst in 0.5 M H_2SO_4, 1.0 M KOH and 1.0 M PBS.

overpotentials of the catalyst at 10 mA·cm^{-2} did not really change over catalytic testing for 30 h. No obvious changes in the composition, morphology and crystalline/electronic structure of the Ru-O-Mn/CPD catalysts were observed after 2000 CV cycles for OER in three media (Fig. S22-24). These results indicate great durability of Ru-O-Mn/CPD for OER under acidic, alkaline and neutral media.

In addition, to further highlight the significant roles of CPD in the distinct crystalline/electronic structures and great OER activity of Ru-O-

Mn/CPD, we prepared pure Ru-O-Mn and Mn-RuO$_2$ with no N-C component incorporated, which are both confirmed by XRD pattern (Fig. S25). Compared to Ru-O-Mn/CPD, there is an obviously broader Ru diffraction signal at ca. 44° observed for pure Ru-O-Mn, but its intensity is lower than RuO$_2$ signals. It indicates the existence of plenty of metallic Ru with low crystallinity. For pure Mn-RuO$_2$, the sharper diffraction perks of RuO$_2$ imply a bigger grain size than Ru-O-Mn/CPD. From Fig. S26a,b, pure Ru-O-Mn and Mn-RuO$_2$ catalysts both display more

Fig. 4. Electrochemical HER performance and overall water-splitting performance of catalysts in 1.0 M KOH media. (a) HER polarization curves for Ru-O-Mn/CPD and control catalysts. (b) HER polarization curves of different Ru-O-M/CPD catalysts and 20% Pt/C. (c) HER activity comparison between Ru-O-Mn/CPD and recently reported state-of-the-art HER electrocatalysts. (d) Polarization curves and (e) durability test of overall water-splitting devices containing Ru-O-Mn/CPD‖Ru-O-Mn/CPD and Pt/C‖RuO$_2$ systems.

inferior acidic and alkaline OER activity than Ru-O-Mn/CPD (Fig. 3a,b). Besides, these two catalysts both display inferior OER durability as shown in Fig. S26c,d.

The OER kinetics of electrocatalysts were studied by the Tafel plot method. From Fig. S27, the Ru-O-Mn/CPD catalyst displays the lowest Tafel slopes of 61.3 mV·dec^{-1} and 59.5 mV·dec^{-1} in 0.5 M H_2SO_4 and 1.0 M KOH media, respectively, implying very favorable OER kinetics. The electrochemical double-layer capacitance (C_{dl}) values of catalysts were obtained from CV curves (Fig. S28,29). As shown in Fig. S30, C_{dl} values of the Ru-O-Mn/CPD catalyst during OER in acid and basic media were 106.1 mF·cm^{-2} and 253.4 mF·cm^{-2}, respectively, higher than the other catalysts. That is, Ru-O-Mn/CPD has the largest electrochemically active surface area (ECSA) for OER. Electrochemical impedance spectroscopy (EIS) spectra (Fig. S31) show that Ru-O-Mn/CPD catalyst had the best catalyst/electrolyte interface charge transfer kinetics among the different catalysts. In addition, the in-situ Raman spectroscopy was carried out to reveal the changes of local electronic structures of Ru-O-Mn/CPD during OER at the potentials ranging from 1.10 V to 1.55 V (vs. RHE) in 1.0 M KOH electrolyte. As shown in Fig. S32, during OER at different applied potentials, there are almost no changes in either intensity or wavenumber position for the characteristic peaks of Ru^{4+} (Ru-O) at 489 cm^{-1}, 615 cm^{-1} and 681 cm^{-1} and Ru^{n+} (n>4) at 820 cm^{-1}. It suggests great stability in the electronic structures of Ru-O-Mn/CPD catalyst during OER.

To get more insights into the modulating effect of Mn sites derived from the Mn-CPDs on the Ru-O sites in Ru-O-Mn/CPD, various Ru-O-M/CPD (M=Cu, Zn, Fe or Co) catalysts were prepared. As displayed in Fig. S33-35, Ru-O-Cu/CPD and Ru-O-Zn/CPD both exhibit a similar crystalline structure and morphology as Ru-O-Mn/CPD. However, for the Ru-O-Fe/CPD and Ru-O-Co/CPD catalysts, Ru^0 sites were not effectively oxidized into Ru-O sites due to stable alloying between Ru and Fe (or Co) (Fig. S33), with obvious aggregation of crystal grains occurring (Fig. S36,37). From the Fig. S38, Ru-O-Cu/CPD and Ru-O-Zn/CPD show excellent OER activity, comparable to Ru-O-Mn/CPD, with η_{10} values of 224 mV and 204 mV in 0.5 M H_2SO_4, and 234 mV and 214 mV in 1.0 M KOH, respectively. Ru-O-Fe/CPD (250 mV and 273 mV) and Ru-O-Co/CPD (230 mV and 247 mV) display decreased OER activity in acidic and basic media, respectively, compared to Ru-O/CPD (225 mV and 230 mV).

Moreover, electrochemical HER performances of catalysts were carried out in a standard three-electrode system in 1.0 M KOH media. From polarization curves (Fig. 4a), Ru-O-Mn/CPD displays the best HER activity with a very low overpotential of 33 mV at 10 mA·cm^{-2} compared with Ru-O/CPD (42 mV) and other catalysts. In addition, Ru-O-Mn/CPD had the highest C_{dl} value (Fig. S39,40) among the different catalysts, reflecting the largest ECSA value. Meanwhile, other Ru-O-M/CPD (M=Cu, Zn or Co) also offer excellent HER activity in 1.0 M KOH media, evidenced by small η_{10} values of only 35 mV, 21 mV and 39 mV, respectively (Fig. 4b). The lower Tafel slopes of these catalysts (Fig. S41) than commercial Pt/C suggest extremely favorable HER kinetics. Indeed, the HER performance for Ru-O-Zn/CPD with an ultralow overpotential ($\eta_{10} =21$ mV) and Tafel slope (20.7 mV·dec^{-1}) was better than commercial Pt/C (29 mV and 24.1 mV·dec^{-1}) and most previously reported many noble metal-based catalysts (Fig. 4c, Table S6). The Ru-O-Mn/CPD and Ru-O-Zn/CPD catalysts both offer good catalytic stability at 10 mA·cm^{-2} during HER in 1.0 M KOH solution (Fig. S42). Also, Fig. S43-45 doesn't display obvious changes in the morphology and electronic structures of the Ru-O-Mn/CPD catalyst after 2000 CV cycles for HER in alkaline media. Then, the in-situ Raman spectroscopy was conducted to further explore the electronic structures of Ru-O-Mn/CPD during HER in 1.0 M KOH electrolyte. From Fig. S46, there are almost no changes for the characteristic peaks of Ru^{4+} (Ru-O) and Ru^{n+} (n>4) during HER at the potentials from 0 V to -0.04 V (vs. RHE). At the more negative potential of -0.04--0.12 V (vs. RHE), the slight shifts for Ru^{4+} (Ru-O) and Ru^{n+} (n>4) peaks can be attributed to the slow reduction of RuO_2 during HER, and a distinct peak at 788 cm^{-1}
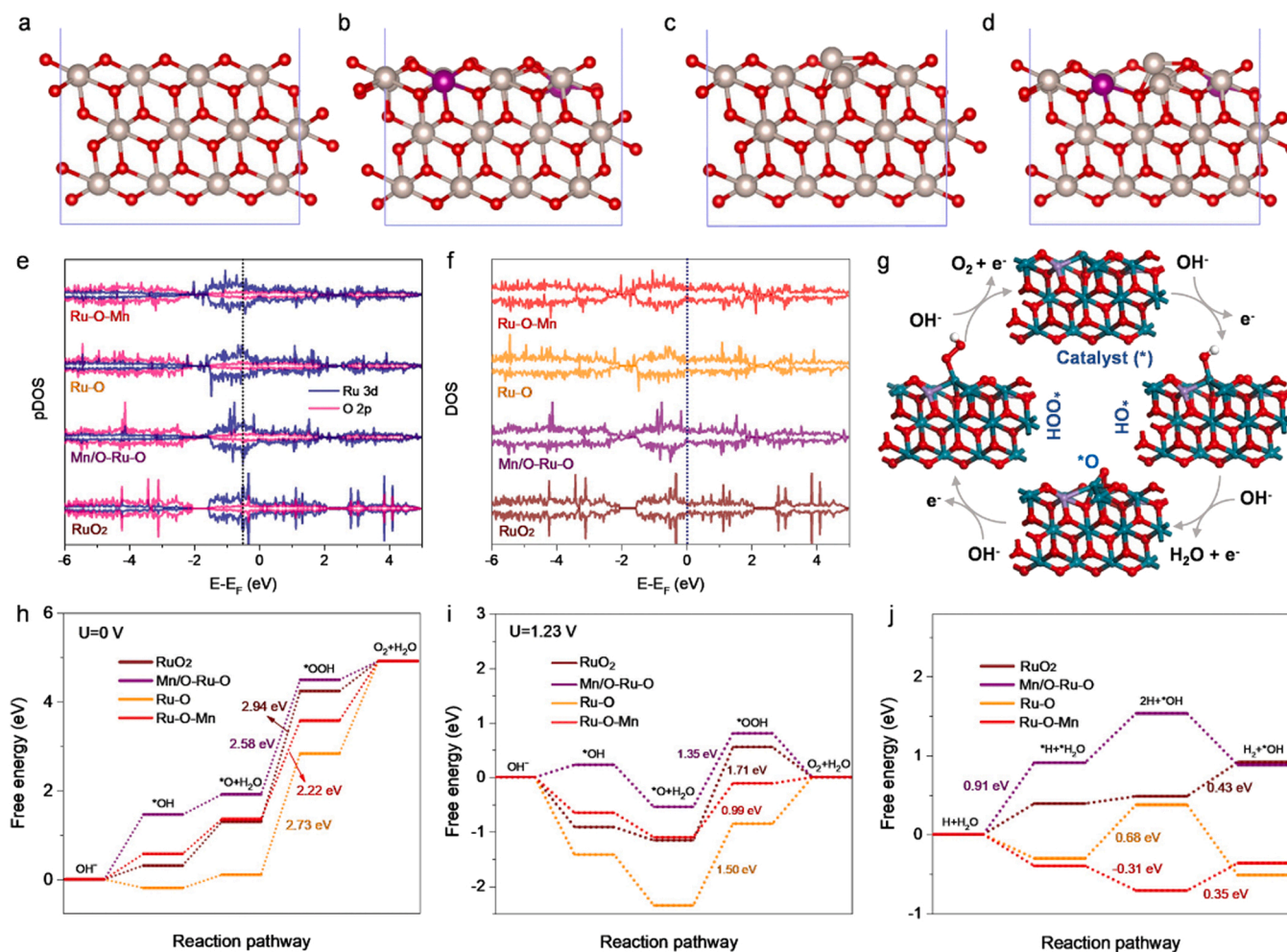
corresponding to the Ru−H bending can be observed, suggesting strong H adsorption by Ru.

Based on the excellent OER/HER performance of the Ru-O-Mn/CPD catalyst in alkaline media, we constructed an overall water-splitting device employing Ru-O-Mn/CPD catalyst as both cathode and anode. Polarization curves (Fig. 4d) demonstrate that Ru-O-Mn/CPD requires an ultralow cell voltage of 1.45 V to deliver 10 mA·cm^{-2} in 1.0 M KOH media. Such overall water-splitting activity is among the best reported for a noble metal-based electrocatalyst (Table S7). The chronopotentiometry test (Fig. 4e) shows that the Ru-O-Mn/CPD-based overall water-splitting device exhibits excellent durability over 40 h. In comparison, a Pt/C ‖ RuO_2 device needs a cell voltage of 1.57 V to achieve 10 mA·cm^{-2} and shows poor durability. Besides, we measured the actual evolution rates of H_2 and O_2 in Ru-O-Mn/CPD-based overall water-splitting device (Fig. S47), with the gases collected by the drainage method. As shown in Fig. S48, the measured H_2 and O_2 evolution amounts are in good agreement with calculated results, which indicates the Faradic efficiencies of H_2 and O_2 evolution are very approximate to 100%. The evolution rates of H_2 and O_2 at 100 mA·cm^{-2} were measured to be 31.8 and 15.6 μmol·min^{-1}, respectively. The measured evolution ratio of H_2 to O_2 is 2.04, which is nearly identical to 2.00, namely the stoichiometric ratio of H_2 to O_2 in the water hydrolysis reaction.

3.3. Density functional theory (DFT) calculation

To gain deeper insights into the excellent OER/HER activity of the Ru-O-Mn/CPD catalyst, density functional theory (DFT) calculations were carried out. Four models, $Ru_{24}O_{48}$, $Ru_{25}O_{48}$, $Ru_{22}Mn_2O_{47}$ and $Ru_{23}Mn_2O_{47}$, were constructed based on the slab model of $RuO_2(101)$ surface as shown in Fig. 5a-d. These models represent the RuO_2, Ru-O/CPD, Mn/O-Ru-O/CPD and Ru-O-Mn/CPD catalysts, respectively. Different oxygen defect numbers were introduced in Ru-O (2), Mn/O-Ru-O (1) and Ru-O-Mn (3) to account for O-Ru-O-Ru-Ru sites and/or incorporated Ru-O-Mn-O units. From the Bader charge analysis (Fig. S49), the partial charge of Ru in pure RuO_2 was calculated to be + 1.66e. The Ru atoms in Ru-O-Mn possess a lower positive charge of + 0.57e. This implies electron transfer from Mn to Ru, (i.e., the formation of electron-rich Ru region), which is in good agreement with XPS and EXAFS results. Further, the presence of O-Ru-O-Ru-Ru sites in catalyst creates an additional electron-rich Ru region. Partial density of states (PDOS) calculation was next performed to investigate the electronic structure of Ru d and O p orbitals. As shown in Fig. 5e, the orbital hybridizations of Ru 4d and O 2p in Ru-O/CPD, Mn/O-Ru-O/CPD and Ru-O-Mn/CPD are enhanced compared to RuO_2. The total DOS of Ru-O/CPD, Mn/O-Ru-O/CPD and Ru-O-Mn/CPD models show a greater carrier concentration and higher intrinsic conductivity compared to RuO_2 (Fig. 5 f). In addition, the DOS spectra show that Ru 4d band center moves from -3.63 eV for RuO_2 to -2.70 eV for Ru-O-Mn due to the presence of Ru-O-Ru-Ru and Ru-O-Mn sites. The shift of the d-band center closer to the Fermi level will enhance the adsorption of molecules. The band center of localized O 2p orbitals is often used as a descriptor to predict the intrinsic OER activity of oxides. The O 2p band center moves from -2.83 eV for RuO_2 to -3.11 eV for Ru-O-Mn, with the energy gap between the O 2p band center and the Fermi level being significantly enlarged. This implies a decreased covalency of the Ru-O bond. These electronic manipulations were clearly responsible for the optimized OER activity of the Ru-O-Mn/CPD catalyst, altering the binding of key intermediates.

In alkaline media, OER proceeds via the formation of HO* , O* , and HOO* intermediates. The optimized structures for different intermediates on the Ru-O-Mn model are shown in Fig. 5 g. According to the calculated free energy diagrams for the OER process (Fig. 5h,i), the formation of *OOH can be regarded as the rate-determining step (RDS). The free energy of the RDS was calculated to be 2.22 eV for the Ru-O-Mn model under U = 0 V, a lower value than on the RuO_2, Ru-O and Mn/O-

Fig. 5. Theoretical models and simulation results. (a-d) The four structure models including $Ru_{24}O_{48}$ (RuO_2), $Ru_{22}Mn_2O_{47}$ (Mn/O-Ru-O), $Ru_{25}O_{48}$ (Ru-O) and $Ru_{23}Mn_2O_{47}$ (Ru-O-Mn). (e-f) The partial and total density of states (DOS) of the four structure models. (g) Four-electron OER pathways on the Ru-O-Mn model in alkaline media. (h, i) Calculated free energy diagrams for alkaline OER pathways on RuO_2, Mn/O-Ru-O, Ru-O and Ru-O-Mn under U= 0 V and U= 1.23 V, respectively. (j) Calculated free energy diagrams for alkaline HER pathways of RuO_2, Mn/O-Ru-O, Ru-O and Ru-O-Mn models.

Ru-O models, suggesting Ru-O-Mn offered an energetically favorable OER pathway. Under U = 1.23 V, the free energy of oxygen intermediate formation is substantially lowered. The Ru-O-Mn model required the smallest overpotential of 0.99 V to overcome the energy barrier for forming *OOH intermediates, which is consistent with experimental results. The result also agrees well with the upshifting of Ru 4d band centers that tune the adsorption energy of oxygen intermediates. For HER in alkaline media (Fig. 5j), the total adsorption energies of *H and H_2O* intermediates on the Ru-O-Mn surface were lower than on the other models. Such moderate adsorption energies close to zero indicate the highest catalytic activity. Over the entire HER pathway, the Ru-O-Mn surface had the smallest reaction energy barrier (0.35 eV), meaning the best alkaline HER activity. The RDS in alkaline HER was water molecule dissociation, with the Ru-O-Mn surface releasing around 0.58 eV in energy for this step, vastly superior to RuO_2, Mn/O-Ru-O and Ru-O (Fig. S50). This indicates that the enhanced HER catalytic activity of Ru-O-Mn/CPD was primarily due to an energetically favorable water dissociation process.

4. Conclusions

In summary, based on the distinct electronic reservoir characters of defective Mn-CPDs, the reduction-oxidation strategy was proposed to controllably fabricate defect-rich Ru-O-Mn/CPD for pH-universal OER. The highly crystalline RuO_2 in Ru-O-Mn/CPD was electronically modified by oxygen-defective sites (including O-Ru-O-Ru-Ru and Ru-O-Mn-O units). These defects acted to precisely tune the electronic properties of Ru cations in Ru-O-Mn/CPD, resulting in outstanding pH-universal OER performance. The theoretical simulation results indicate that these defect-rich Ru-O sites form electron-rich Ru region and modulate the Ru-4d/O-2p band center, resulting in optimized binding of OER intermediates. The Ru-O-Mn/CPD electrocatalyst shows ultralow OER overpotentials of 196 mV, 194 mV and 251 mV at 10 mA·cm^{-2} in 0.5 M H_2SO_4, 1.0 M KOH, and neutral 1.0 M PBS media, respectively, along with excellent Pt/C-like HER performance. In an overall water-splitting device, Ru-O-Mn/CPD required a cell voltage of only 1.45 V to deliver 10 mA·cm^{-2} in 1.0 M KOH media. This study paves a new avenue to designing high-performance pH-universal oxygen evolution electrocatalyst for water splitting.

CRediT authorship contribution statement

Tanglue Feng: Conceptualization, Methodology, Investigation, Visualization, Data curation, Formal analysis, Visualization, Writing – original draft, Writing – review & editing. **Jingkun Yu:** Investigation on DFT calculation and corresponding analysis and writing. **Da Yue:** Investigation, Data curation, Paper editing. **Haoqiang Song:** Data analysis and Paper editing. **Songyuan Tao:** Writing – review & editing. **Geoffrey I.N. Waterhouse:** Writing – review & editing. **Siyu Lu:** Conceptualization, DFT calculation, Project administration, Writing –

review & editing. **Bai Yang:** Conceptualization, Visualization, Leading, Project administration, Funding acquisition, Writing – review & editing, Finalization.

Declaration of Competing Interest

The authors declare that they have no known competing financial interests or personal relationships that could have appeared to influence the work reported in this paper.

Data Availability

Data will be made available on request.

Acknowledgement

Appendix A. Supporting information

Supplementary data associated with this article can be found in the online version at doi:10.1016/j.apcatb.2023.122546.

References

[1] Q. Shi, C. Zhu, D. Du, Y. Lin, Robust noble metal-based electrocatalysts for oxygen evolution reaction, Chem. Soc. Rev. 48 (2019) 3181–3192, https://doi.org/10.1039/C8CS00671G.

[2] J. Yin, J. Jin, M. Lu, B. Huang, H. Zhang, Y. Peng, P. Xi, C.H. Yan, Iridium single atoms coupling with oxygen vacancies boosts oxygen evolution reaction in acid media, J. Am. Chem. Soc. 142 (2020) 18378–18386, https://doi.org/10.1021/jacs.0c05050.

[3] H.N. Nong, T. Reier, H.-S. Oh, M. Gliech, P. Paciok, T.H.T. Vu, D. Teschner, M. Heggen, V. Petkov, R. Schlögl, T. Jones, P. Strasser, A unique oxygen ligand environment facilitates water oxidation in hole-doped IrNiOx core–shell electrocatalysts, Nat. Catal. 1 (2018) 841–851, https://doi.org/10.1038/s41929-018-0153-y.

[4] N.T. Suen, S.F. Hung, Q. Quan, N. Zhang, Y.J. Xu, H.M. Chen, Electrocatalysis for the oxygen evolution reaction: recent development and future perspectives, Chem. Soc. Rev. 46 (2017) 337–365, https://doi.org/10.1039/C6CS00328A.

[5] Z.P. Wu, X.F. Lu, S.Q. Zang, X.W. Lou, Non-noble-metal-based electrocatalysts toward the oxygen evolution reaction, Adv. Funct. Mater. 30 (2020), 1910274, https://doi.org/10.1002/adfm.201910274.

[6] J. Zhang, Q. Zhang, X. Feng, Support and interface effects in water-splitting electrocatalysts, Adv. Mater. 31 (2019), e1808167, https://doi.org/10.1002/adma.201808167.

[7] D. Zhou, S. Wang, Y. Jia, X. Xiong, H. Yang, S. Liu, J. Tang, J. Zhang, D. Liu, L. Zheng, Y. Kuang, X. Sun, B. Liu, NiFe hydroxide lattice tensile strain: enhancement of adsorption of oxygenated intermediates for efficient water oxidation catalysis, Angew. Chem. Int. Ed. 58 (2019) 736–740, https://doi.org/10.1002/anie.201809689.

[8] X. Bo, R.K. Hocking, S. Zhou, Y. Li, X. Chen, J. Zhuang, Y. Du, C. Zhao, Capturing the active sites of multimetallic (oxy)hydroxides for the oxygen evolution reaction, Energy Environ. Sci. 13 (2020) 4225–4237, https://doi.org/10.1039/D0EE01609H.

[9] C. Kuai, Z. Xu, C. Xi, A. Hu, Z. Yang, Y. Zhang, C.-J. Sun, L. Li, D. Sokaras, C. Dong, S.-Z. Qiao, X.-W. Du, F. Lin, Phase segregation reversibility in mixed-metal hydroxide water oxidation catalysts, Nat. Catal. 3 (2020) 743–753, https://doi.org/10.1038/s41929-020-0496-z.

[10] S. Li, Y. Gao, N. Li, L. Ge, X. Bu, P. Feng, Transition metal-based bimetallic MOFs and MOF-derived catalysts for electrochemical oxygen evolution reaction, Energy Environ. Sci. 14 (2021) 1897–1927, https://doi.org/10.1039/D0EE03697H.

[11] J. Liang, X. Gao, B. Guo, Y. Ding, J. Yan, Z. Guo, E.C.M. Tse, J. Liu, Ferrocene-based metal-organic framework nanosheets as a robust oxygen evolution catalyst, Angew. Chem. Int. Ed. 60 (2021) 12770–12774, https://doi.org/10.1002/anie.202101878.

[12] N. Wang, S. Ning, X. Yu, D. Chen, Z. Li, J. Xu, H. Meng, D. Zhao, L. Li, Q. Liu, B. Lu, S. Chen, Graphene composites with Ru-RuO2 heterostructures: Highly efficient Mott–Schottky-type electrocatalysts for pH-universal water splitting and flexible zinc–air batteries, Appl. Catal. B: Environ. 302 (2022), 120838, https://doi.org/10.1016/j.apcatb.2021.120838.

[13] F. Luo, L. Guo, Y. Xie, J. Xu, K. Qu, Z. Yang, Iridium nanorods as a robust and stable bifunctional electrocatalyst for pH-universal water splitting, Appl. Catal. B: Environ. 279 (2020), 119394, https://doi.org/10.1016/j.apcatb.2020.119394.

[14] Z. Lei, T. Wang, B. Zhao, W. Cai, Y. Liu, S. Jiao, Q. Li, R. Cao, M. Liu, Recent progress in electrocatalysts for acidic water splitting, Adv. Energy Mater. 10 (2020), 2000478, https://doi.org/10.1002/aenm.202000478.

[15] L. Gloag, T.M. Benedetti, S. Cheong, Y. Li, X.H. Chan, L.M. Lacroix, S.L.Y. Chang, R. Arenal, I. Florea, H. Barron, A.S. Barnard, A.M. Henning, C. Zhao, W. Schuhmann, J.J. Gooding, R.D. Tilley, Three-dimensional branched and faceted gold-ruthenium nanoparticles: using nanostructure to improve stability in oxygen evolution electrocatalysis, Angew. Chem. Int. Ed. 57 (2018) 10241–10245, https://doi.org/10.1002/anie.201806300.

[16] Y. Lin, Z. Tian, L. Zhang, J. Ma, Z. Jiang, B.J. Deibert, R. Ge, L. Chen, Chromium-ruthenium oxide solid solution electrocatalyst for highly efficient oxygen evolution reaction in acidic media, Nat. Commun. 10 (2019) 162, https://doi.org/10.1038/s41467-018-08144-3.

[17] S. Chen, H. Huang, P. Jiang, K. Yang, J. Diao, S. Gong, S. Liu, M. Huang, H. Wang, Q. Chen, Mn-doped RuO2 nanocrystals as highly active electrocatalysts for enhanced oxygen evolution in acidic media, ACS Catal. 10 (2019) 1152–1160, https://doi.org/10.1021/acscatal.9b04922.

[18] J. Su, R. Ge, K. Jiang, Y. Dong, F. Hao, Z. Tian, G. Chen, L. Chen, Assembling ultrasmall copper-doped ruthenium oxide nanocrystals into hollow porous polyhedra: highly robust electrocatalysts for oxygen evolution in acidic media, Adv. Mater. (2018), e1801351, https://doi.org/10.1002/adma.201801351.

[19] H. Sun, W. Jung, Recent advances in doped ruthenium oxides as high-efficiency electrocatalysts for the oxygen evolution reaction, J. Mater. Chem. A 9 (2021) 15506–15521, https://doi.org/10.1039/D1TA03452A.

[20] Y. Tian, S. Wang, E. Velasco, Y. Yang, L. Cao, L. Zhang, X. Li, Y. Lin, Q. Zhang, L. Chen, A Co-doped nanorod-like RuO2 electrocatalyst with abundant oxygen vacancies for acidic water oxidation, iScience 23 (2020), 100756, https://doi.org/10.1016/j.isci.2019.100756.

[21] S. Hao, M. Liu, J. Pan, X. Liu, X. Tan, N. Xu, Y. He, L. Lei, X. Zhang, Dopants fixation of ruthenium for boosting acidic oxygen evolution stability and activity, Nat. Commun. 11 (2020) 5368, https://doi.org/10.1038/s41467-020-19212-y.

[22] Y. Xue, J. Fang, X. Wang, Z. Xu, Y. Zhang, Q. Lv, M. Liu, W. Zhu, Z. Zhuang, Sulfate-functionalized RuFeOx as highly efficient oxygen evolution reaction electrocatalyst in acid, Adv. Funct. Mater. 31 (2021), 2101405, https://doi.org/10.1002/adfm.202101405.

[23] J. He, W. Li, P. Xu, J. Sun, Tuning electron correlations of RuO2 by co-doping of Mo and Ce for boosting electrocatalytic water oxidation in acidic media, Appl. Catal. B: Environ. 298 (2021), 120528, https://doi.org/10.1016/j.apcatb.2021.120528.

[24] S. Niu, X.-P. Kong, S. Li, Y. Zhang, J. Wu, W. Zhao, P. Xu, Low Ru loading RuO2/(Co,Mn)3O4 nanocomposite with modulated electronic structure for efficient oxygen evolution reaction in acid, Appl. Catal. B: Environ. 297 (2021), 120442, https://doi.org/10.1016/j.apcatb.2021.120442.

[25] W. Li, D. Wang, Y. Zhang, L. Tao, T. Wang, Y. Zou, Y. Wang, R. Chen, S. Wang, Defect engineering for fuel-cell electrocatalysts, Adv. Mater. 32 (2020), e1907879, https://doi.org/10.1002/adma.201907879.

[26] Y. Jia, K. Jiang, H. Wang, X. Yao, The role of defect sites in nanomaterials for electrocatalytic energy conversion, Chem 5 (2019) 1371–1397, https://doi.org/10.1016/j.chempr.2019.02.008.

[27] Q. Wang, Y. Lei, D. Wang, Y. Li, Defect engineering in earth-abundant electrocatalysts for CO2 and N2 reduction, Energy Environ. Sci. 12 (2019) 1730–1750, https://doi.org/10.1039/C8EE03781G.

[28] Y. Li, Y. Wang, J. Lu, B. Yang, X. San, Z.-S. Wu, 2D intrinsically defective RuO2/Graphene heterostructures as All-pH efficient oxygen evolving electrocatalysts with unprecedented activity, Nano Energy 78 (2020), 105185, https://doi.org/10.1016/j.nanoen.2020.105185.

[29] L. Zhang, H. Jang, H. Liu, M.G. Kim, D. Yang, S. Liu, X. Liu, J. Cho, Sodium-decorated amorphous/crystalline RuO2 with rich oxygen vacancies: a robust pH-universal oxygen evolution electrocatalyst, Angew. Chem. Int. Ed. 60 (2021) 18821–18829, https://doi.org/10.1002/anie.202106631.

[30] C.-B. Hong, X. Li, W.-B. Wei, X.-T. Wu, Q.-L. Zhu, Nano-engineering of Ru-based hierarchical porous nanoreactors for highly efficient pH-universal overall water splitting, Appl. Catal. B: Environ. 294 (2021), 120230, https://doi.org/10.1016/j.apcatb.2021.120230.

[31] H.-S. Park, J. Yang, M.K. Cho, Y. Lee, S. Cho, S.-D. Yim, B.-S. Kim, J.H. Jang, H.-K. Song, RuO2 nanocluster as a 4-in-1 electrocatalyst for hydrogen and oxygen electrochemistry, Nano Energy 55 (2019) 49–58, https://doi.org/10.1016/j.nanoen.2018.10.017.

[32] J. Yang, L. Chang, H. Guo, J. Sun, J. Xu, F. Xiang, Y. Zhang, Z. Wang, L. Wang, F. Hao, X. Niu, Electronic structure modulation of bifunctional oxygen catalysts for rechargeable Zn-air batteries, J. Mater. Chem. A 8 (2020) 1229–1237, https://doi.org/10.1039/C9TA11654K.

[33] Y. Lee, J.H. Ahn, S. Shin, S.-H. Jung, H.-S. Park, Y.-G. Cho, D.-G. Lee, H. Kong, J.H. Lee, H.-K. Song, Metal-nitrogen intimacy of the nitrogen-doped ruthenium oxide for facilitating electrochemical hydrogen production, Appl. Catal. B: Environ. 303 (2022), 120873, https://doi.org/10.1016/j.apcatb.2021.120873.

[34] R. Ge, L. Li, J. Su, Y. Lin, Z. Tian, L. Chen, Ultrafine defective RuO2 electrocatayst integrated on carbon cloth for robust water oxidation in acidic media, Adv. Energy Mater. 9 (2019), 1901313, https://doi.org/10.1002/aenm.201901313.

[35] G. Zhang, B. Wang, L. Li, S. Yang, J. Liu, S. Yang, Tailoring the electronic structure by constructing the heterointerface of RuO2–NiO for overall water splitting with ultralow overpotential and extra-long lifetime, J. Mater. Chem. A 8 (2020) 18945–18954, https://doi.org/10.1039/D0TA06565J.

[36] J. Wang, Y. Ji, R. Yin, Y. Li, Q. Shao, X. Huang, Transition metal-doped ultrathin RuO2 networked nanowires for efficient overall water splitting across a broad pH

range, J. Mater. Chem. A 7 (2019) 6411–6416, https://doi.org/10.1039/C9TA00598F.

[37] H. Over, Surface chemistry of ruthenium dioxide in heterogeneous catalysis and electrocatalysis: from fundamental to applied research, Chem. Rev. 112 (2012) 3356–3426, https://doi.org/10.1021/cr200247n.

[38] M. Etzi Coller Pascuzzi, A. Goryachev, J.P. Hofmann, E.J.M. Hensen, Mn promotion of rutile TiO2-RuO2 anodes for water oxidation in acidic media, Appl. Catal. B: Environ. 261 (2020), 118225, https://doi.org/10.1016/j.apcatb.2019.118225.

[39] C. Hu, M. Li, J. Qiu, Y.P. Sun, Design and fabrication of carbon dots for energy conversion and storage, Chem. Soc. Rev. 48 (2019) 2315–2337, https://doi.org/10.1039/C8CS00750K.

[40] V.C. Hoang, K. Dave, V.G. Gomes, Carbon quantum dot-based composites for energy storage and electrocatalysis: mechanism, applications and future prospects, Nano Energy 66 (2019), 104093, https://doi.org/10.1016/j.nanoen.2019.104093.

[41] W. Li, Y. Liu, M. Wu, X. Feng, S.A.T. Redfern, Y. Shang, X. Yong, T. Feng, K. Wu, Z. Liu, B. Li, Z. Chen, J.S. Tse, S. Lu, B. Yang, Carbon-quantum-dots-loaded ruthenium nanoparticles as an efficient electrocatalyst for hydrogen production in alkaline media, Adv. Mater. 30 (2018), e1800676, https://doi.org/10.1002/adma.201800676.

[42] Y. Zhai, B. Zhang, R. Shi, S. Zhang, Y. Liu, B. Wang, K. Zhang, G.I.N. Waterhouse, T. Zhang, S. Lu, Carbon dots as new building blocks for electrochemical energy storage and electrocatalysis, Adv. Energy Mater. 12 (2021), 2103426, https://doi.org/10.1002/aenm.202103426.

[43] H. Song, Y. Li, L. Shang, Z. Tang, T. Zhang, S. Lu, Designed controllable nitrogen-doped carbon-dots-loaded MoP nanoparticles for boosting hydrogen evolution reaction in alkaline medium, Nano Energy 72 (2020), 104730, https://doi.org/10.1016/j.nanoen.2020.104730.

[44] T. Feng, S. Tao, D. Yue, Q. Zeng, W. Chen, B. Yang, Recent advances in energy conversion applications of carbon dots: from optoelectronic devices to electrocatalysis, Small 16 (2020), e2001295, https://doi.org/10.1002/smll.202001295.

[45] Y. Cai, J. Fu, Y. Zhou, Y.C. Chang, Q. Min, J.J. Zhu, Y. Lin, W. Zhu, Insights on forming N,O-coordinated Cu single-atom catalysts for electrochemical reduction CO2 to methane, Nat. Commun. 12 (2021) 586, https://doi.org/10.1038/s41467-020-20769-x.

[46] M. Yang, T. Feng, Y. Chen, J. Liu, X. Zhao, B. Yang, Synchronously integration of Co, Fe dual-metal doping in Ru@C and CDs for boosted water splitting performances in alkaline media, Appl. Catal. B: Environ. 267 (2020), 118657, https://doi.org/10.1016/j.apcatb.2020.118657.

[47] Y. Liu, X. Li, Q. Zhang, W. Li, Y. Xie, H. Liu, L. Shang, Z. Liu, Z. Chen, L. Gu, Z. Tang, T. Zhang, S. Lu, A general route to prepare low-ruthenium-content bimetallic electrocatalysts for pH-universal hydrogen evolution reaction by using carbon quantum dots, Angew. Chem. Int. Ed. 59 (2020) 1718–1726, https://doi.org/10.1002/anie.201913910.

[48] T. Feng, G. Yu, S. Tao, S. Zhu, R. Ku, R. Zhang, Q. Zeng, M. Yang, Y. Chen, W. Chen, W. Chen, B. Yang, A highly efficient overall water splitting ruthenium-cobalt alloy electrocatalyst across a wide pH range via electronic coupling with carbon dots, J. Mater. Chem. A 8 (2020) 9638–9645, https://doi.org/10.1039/D0TA02496A.

[49] L. Lin, L. Luo, P. Tsai, J. Wang, X. Chen, Metal ions doped carbon quantum dots: Synthesis, physicochemical properties: and their applications, TrAC-Trend Anal. Chem. 103 (2018) 87–101, https://doi.org/10.1016/j.trac.2018.03.015.

[50] X. Li, Y. Fu, S. Zhao, J. Xiao, M. Lan, B. Wang, K. Zhang, X. Song, L. Zeng, Metal ions-doped carbon dots: Synthesis, properties, and applications, Chem. Eng. J. 430 (2022), 133101, https://doi.org/10.1016/j.cej.2021.133101.